Observing posteruptive deflation of hydrothermal system using InSAR time series analysis: An application of ALOS-2/PALSAR-2 data on the 2015 phreatic eruption of Hakone volcano, Japan

Ryosuke Doke[1,2], Kazutaka Mannen[2,2], and Kazuhiro Itadera[1,2]

[1]Hot Springs Research Institute, Kanagawa Prefecture
[2]Hot Springs Research Institute of Kanagawa Prefecture

November 30, 2022

Abstract

From 29 June to 1 July, 2015, a phreatic eruption occurred in Owakudani, the largest fumarole area in Hakone volcano, Japan. In this study, an interferometric synthetic aperture radar (InSAR) time series analysis of the Advanced Land Observing Satellite-2 (ALOS-2)/Phased Array type L-band Synthetic Aperture Radar-2 (PALSAR-2) data was performed to measure deformation after the eruption. The results show that the central cones of the volcano have subsided since the eruption and its deflation source is located beneath the previously estimated bell-shaped conductor, which is considered as a sealing layer confining a pressurized hydrothermal reservoir. Therefore, the InSAR results demonstrate the deflation of the hydrothermal system beneath the volcano. One possible cause of this deflation is compaction due to a decrease in pore pressure caused by rupture and fluid migration during and after the eruption.

Observing posteruptive deflation of hydrothermal system using InSAR time series analysis: An application of ALOS-2/PALSAR-2 data on the 2015 phreatic eruption of Hakone volcano, Japan

by R. Doke[1], K. Mannen[1], and K. Itadera[1]

[1] Hot Springs Research Institute of Kanagawa Prefecture, 586 Iriuda, Odawara, Kanagawa 250-0031, Japan.

Corresponding author: Ryosuke Doke (r-doke@onken.odawara.kanagawa.jp)

Key Points:

- Posteruptive deflation beneath the central cones of Hakone volcano was detected by radar interferometry after the 2015 phreatic eruption
- Our model inversion suggests that deflation of a hydrothermal system confined by a sealing layer beneath the volcano has been taking place
- The hydrothermal system deflation is likely attributable to rupture of the sealing layer and system depressurization due to the eruption

Abstract

From 29 June to 1 July, 2015, a phreatic eruption occurred in Owakudani, the largest fumarole area in Hakone volcano, Japan. In this study, an interferometric synthetic aperture radar (InSAR) time series analysis of the Advanced Land Observing Satellite-2 (ALOS-2)/Phased Array type L-band Synthetic Aperture Radar-2 (PALSAR-2) data was performed to measure deformation after the eruption. The results show that the central cones of the volcano have subsided since the eruption and its deflation source is located beneath the previously estimated bell-shaped conductor, which is considered as a sealing layer confining a pressurized hydrothermal reservoir. Therefore, the InSAR results demonstrate the deflation of the hydrothermal system beneath the volcano. One possible cause of this deflation is compaction due to a decrease in pore pressure caused by rupture and fluid migration during and after the eruption.

Plain Language Summary

From 29 June to 1 July, 2015, an eruption occurred in Owakudani, the largest steaming area in Hakone volcano, Japan. Our analysis using satellite radar demonstrates that the central part of Hakone volcano has subsided since the eruption and that the deflation source is located in the reservoir of hot water beneath the volcano. One possible cause of this deflation is compaction due to a pressure drop produced by rupture and fluid migration during and after the eruption.

1 Introduction

Measurements of crustal deformation in volcanic regions play an important role in volcano monitoring. With the recent development of synthetic aperture radar (SAR) technology, posteruptive deflation has been observed after phreatic eruptions in various volcanoes (e.g., Hamling et al., 2016; Himematsu et al., 2020; Narita & Murakami, 2018). Volcanic deflation, which occurs at different temporal and spatial scales, is explained by various factors, such as decreases in pore pressure resulting from fluid migration (e.g., Todesco et al., 2014; Wang et al., 2019) and thermoelastic responses with cooling (e.g., Furuya, 2005; Wang & Aoki, 2019). Constraining the source of posteruptive deflation is important when evaluating the structure and physical properties of hydrothermal systems beneath volcanoes and assessing the risk of future phreatic eruptions and signals during volcanic unrest. However, the relationship between the deflation source and the structure of the hydrothermal system based on preexisting subsurface surveys has not been sufficiently discussed in previous studies. Recent magnetotelluric surveys have revealed the structure of the hydrothermal system beneath Hakone volcano, the focal point of this study, providing an appropriate context within which to discuss this topic.

Hakone is a caldera volcano located approximately 100 km west of Tokyo, the capital of Japan (Figure 1). This volcano has been active for more than 400 ky, and effusive eruptions of andesitic magma in the past 40 ky have formed its central cones (e.g., Mts. Kamiyama and Komagatake in Figure 1) (Geological Society of Japan, 2007). Since its latest magmatic eruption (3 ka), several phreatic eruptions have occurred near Owakudani, the largest fumarole area of the volcano, which was formed on the foot of the latest edifice (Kobayashi et al., 2006; Kobayashi, 2008; Tsuchiya et al., 2017). Since the beginning of the 21st century, volcanic unrest has occurred every few years. The unrest that began in April 2015 was the largest in terms of seismicity in the history of modern observation since 1960. The 2015 unrest culminated in a small phreatic eruption on 29 June in Owakudani, which released 80–130 tons of ash and ballistic clasts (Furukawa et al., 2015). Although the 2015 phreatic eruption was small in scale, a dense network of instrumental observation sites detected detailed processes of earthquake activity and crustal deformation during the unrest (e.g., Harada et al., 2018; Honda et al., 2018; Yukutake et al., 2017).

The observation during the preeruptive unrest suggests a deep (>6 km) supply of fluid, which was detected as an inflation of the volcanic edifice and a swarm of deep low-frequency events, initiated in early April 2015 (Harada et al., 2018; Yukutake et al., 2019). Then shallow (<6 km) pressurization of the hydrothermal system was implied from an earthquake swarm that occurred beneath the central cones from the end of April, and abnormal steaming activity from a steam production well (SPW) in Owakudani (500 m deep with a well mouth elevation of 1000 m) occurred in early May (Mannen et al., 2018; Yukutake et al., 2017). The area within 200 m of the SPW showed local swelling, which was detected by an interferometric SAR (InSAR) analysis of Advanced Land Observing Satellite-2 (ALOS-2)/Phased Array type L-band Synthetic Aperture Radar-2 (PALSAR-2) data (Doke et al., 2018; Kobayashi et al., 2018). The phreatic eruption occurred near the southern edge of the swelling area from 29 June to 1 July 2015 (Kobayashi et al., 2018). The InSAR analysis of ALOS-2/PALSAR-2 pairs before and after the phreatic eruption has demonstrated surface displacements caused by the opening of an NW–SE-trending crack formed deeper than 830 m above sea level and the closing of a sill beneath the crack, approximately 225 m above sea level (Doke et al., 2018). Although InSAR has poor time resolution, Honda et al. (2018) also estimated an NW–SE-trending crack from a rapid tilt change over the course of 2 min starting at 07:33 JST on 29 June 2015. These lines of evidence indicate that the phreatic eruption was triggered by hydrothermal fluids stored approximately 225 m above sea level, which migrated toward the shallower part of the edifice through the crack during the eruption. Since the 2015 phreatic eruption, fumarolic activity in Owakudani has been higher than before (Mannen et al., 2021). This higher steam activity during and after the eruption suggests the rupturing of the sealed and pressured hydrothermal system beneath the volcano during the 2015 eruption, as indicated by general modeling of hydrothermal systems (e.g., Fournier, 1999; Stix & de Moor, 2018).

Regarding the location of Hakone volcano, there are residential areas within 1 km of Owakudani, the possible eruption center, so even a small-scale eruption would cause significant damage. Although forecasting phreatic eruptions is known to be challenging, it may be possible to monitor the hydrothermal system located in the shallow regions of the volcano using InSAR. In this study, we performed an InSAR time series analysis of the ALOS-2/PALSAR-2 data to clarify the surface velocities after the 2015 phreatic eruption of Hakone volcano. Applying the inversion technique to the surface velocities, we modeled the deflation sources, and the cause of this deflation is discussed here.

2 Data and Methods

The PALSAR-2 is a multi-mode and right- and left-looking SAR sensor aboard the ALOS-2 launched by the Japan Aerospace Exploration Agency (JAXA) (Rosenqvist et al., 2014). Its wavelength is 23.8 cm (L-band). The datasets selected for this study are path 126 (ascending orbit, right-looking) and path 18 (descending orbit, right-looking), which include observations of Hakone volcano. These paths have the largest number of observation data of any ascending or descending orbit, respectively, from 2 July 2015 to 1 April 2021, which is the period after the phreatic eruption. Thus, it is expected that many interference pairs can be obtained, allowing for greater precision in the analysis. Paths 126 and 18 represent observations from the west and east sides of the sky, respectively, and their off-nadir angles are 38.7° and 38.9°, respectively. The data extracted for this study are given in Table S1. InSAR time series analysis based on the small baseline subset (SBAS) method (Berardino et al., 2002) was used to remove noise, such as atmospheric effects. For the SBAS-InSAR time series analysis, interference pairs, whose time intervals are within 365 days, were extracted for each path. Path 126 has 21 extracted scenes and 74 pairs, whereas path 18 has 24 extracted scenes and 85 pairs. The time–baseline plots are shown in Figure S1.

ENVI SARscape software was used for the SBAS-InSAR time series analysis. The analysis area was cut out from the original data to focus on Hakone volcano and reduce the analysis time (Figure 1). The data were averaged over 11 by 14 looks in the range and azimuth directions, respectively (corresponding to an area of approximately 25 m by 25 m), to improve the signal-to-noise ratio. The influence of the topography in initial interferograms was removed using ellipsoidal height, generated from a 10-m digital elevation model (DEM) released by the Geospatial Information Authority of Japan and Earth Gravitational Model 2008 geoid heights (Pavlis et al., 2012). An adaptive filter (Goldstein and Werner, 1998) was used to reduce the noise, and the interferograms were unwrapped by the minimum-cost flow approach (Costantini, 1998) with a 0.25 coherence threshold. For the removal of orbital residuals, 150 points of ground control point were set as good coherence points in the area, except at the central cones of Hakone volcano, in which significant displacements were observed, and a polynomial surface was assumed. For the inversion of the SBAS-InSAR time series analysis (Berardino et al., 2002), a linear displacement model was used. Atmospheric effects were estimated by applying a spatial low-pass filter with a cutoff of 1,200 m and a temporal high-pass filter with a cutoff of 365 days. Finally, the estimated surface velocities were geocoded to the geographic coordinates in WGS-84, and surface velocity maps were obtained with a resolution of 25 m by 25 m. Moreover, Quasi-eastward and quasi-upward components were calculated by 2.5-D analysis (Fujiwara et al., 2000).

3 Results

Figures 2(a) and (b) show surface velocity maps after the 2015 phreatic eruption estimated by the SBAS-InSAR time series analysis. The velocities are indicated in the line-of-sight (LOS) directions, and positive and negative values indicate velocities toward and away from the satellite, respectively. An area of 2 km in diameter, located at the central cones of the volcano, shows subsidence in the quasi-upward component, and its velocity is below −10 mm/yr (Figure 2 (d)). Since the atmospheric conditions in the study area are varied locally, the effects may not have been fully eliminated by the analysis. However, the observed velocity is significantly greater than the component correlated with topography, suggesting subsidence at the central cones.

Figure 3 shows the time variation of displacements at the selected locations A and B in Figure 2. Location A was selected in the Sengokuhara area (Figure 1), located on the caldera floor far from the central cones of the volcano, and location B was selected near the central cones. Although location A did not show any significant displacement, location B was displaced in the negative LOS direction (away from the satellite) during the analysis period, except for 2019 at Path 126. These results show that the central cones (location B) had significantly subsided with respect to location A. The vertical velocity at location B is approximately −18.3

mm/yr (Figure 2(d)). The displacement pattern in 2019 might have been affected by volcanic unrest.

Significant displacement was detected near Owakudani, and this area was evaluated as location C. Location C showed the maximum velocity in the negative LOS direction on path 18 with a velocity of approximately −43.5 mm/yr (Figures 2(b) and 3(b)). However, the equivalent displacement was not detected on path 126 (Figure 3(a)). This velocity was considered to be due to a landslide because it shows the local displacement near Owakudani and is located on a slope steeply inclined toward the northwest (the negative LOS direction on path 18). Assuming that the displacement is in the inclination direction of the slope, the velocity is estimated to be 51.9 mm/yr. Moreover, a seasonal pattern was observed at Location C (Figure 3(b)), suggesting that the landslide displacement was accelerated by precipitation and other factors.

Model inversion was conducted to explain the surface velocity distributions obtained from the SBAS-InSAR time series analysis (see Text S1 and Figures S2-5). Two deflation source models were used: a point pressure source model (Mogi, 1958) and a rectangular sill model (tensile fault model by Okada, 1985) in a semi-infinite elastic crust. The optimal parameters for each model are given in Table 1 with their standard errors. Moreover, the root mean square (RMS) and Akaike's information criterion (AIC) values for each model are also given in Table 1. The point source deflation model, which had a volume change rate of -5.96×10^4 m^3/yr, was estimated beneath the central cones of Hakone volcano at an altitude of 211.0 m above sea level. Additionally, the rectangular sill deflation model with a long side along the NW–SE direction was estimated at 95.0 m above sea level, and its opening rate was −0.111 m/yr (closing). The volume change rate of the sill deflation model was calculated to be -6.54×10^4 m^3/yr. Although the RMS and AIC values for the sill deflation model are slightly smaller than those for the point source deflation model, both models can explain the patterns of the surface velocities (Figure S2).

4 Discussion and Conclusion

Recent magnetotelluric surveys of Hakone volcano have reported the existence of a bell-shaped conductor (<10 Ωm) beneath the central cones of the volcano (Mannen et al., 2019; Seki et al., 2020; Yoshimura et al., 2018). Similar bell-shaped conductors have been detected in other volcanoes (e.g., Komori et al., 2013; Nurhasan et al., 2006; Usui et al., 2017) and interpreted as impermeable layers that contain smectite, a very conductive altered mineral formed by hydrothermal activity (e.g., Lévy et al., 2018; Pellerin et al., 1996). Moreover, these impermeable layers are considered to be sealing layers that confine pressurized hydrothermal systems beneath volcanoes, which can cause phreatic eruptions (e.g., Stix & de Moor, 2018). Based on a controlled-source audio-frequency magnetotellurics (CSAMT) survey and geological analysis, Mannen et al. (2019) indicated that a portion just beneath the bell-shaped conductor forms a vapor–liquid coexisting hydrothermal system. The area surrounded by the bell-shaped conductor in a wider range of resistivity structure estimated by Yoshimura et al. (2018) agrees well with the subsidence area (Figure 2(d)). Moreover, Seki et al. (2021) showed that the bottom of the bell-shaped conductor beneath the central cones of Hakone volcano is approximately 600–700 m above sea level so that the posteruptive deflation source is located beneath the bell-shaped conductor (about 100–200 m above sea level; Figure 4). Therefore, the results of this study demonstrate that deflation has been occurring in the hydrothermal system beneath the volcano.

Based on the heat flux of 20 MW before the 2015 phreatic eruption in Owakudani (Mannen et al., 2018), the release rate for water vapor is estimated to be 2.8×10^8 kg/yr (1 atm, 100 °C). Alternatively, the deflation rates (5.96×10^4–6.54×10^4 m^3/yr) for the models in this study can be converted to water loss rates of 4.1×10^7–4.5×10^7 kg/yr, assuming the water density (690 kg/m^3) at the boiling point (311 °C) for the pore pressure at the given depth (10 MPa). This means even preeruptive water release at Owakudani was at least 6–7 times larger than the water loss of the hydrothermal system implied from our InSAR time series analysis. After the eruption, the release of water vapor can be considered to be several times greater than the preeruptive release. Therefore, the posteruptive deflation source was not regarded as the principal source of posteruptive fumarole activity, and the hydrothermal fluids are supplied from a deeper part.

So what is the cause of the posteruptive deflation in Hakone volcano? One possible cause of posteruptive deflation is compaction due to a decrease in pore pressure (Todesco et al., 2014; Wang et al., 2019). Because the behavior of crustal deformations during the 2015 phreatic eruption suggests fluid migration from the hydrothermal reservoir to a shallower edifice (Doke et al., 2018), the preeruptive pore pressure could have been released during and after the migration (Figure 4). Moreover, in the shallow part of Owakudani, a posteruptive enlargement of the high-resistivity zone (>10 Ωm) was detected (Mannen et al., 2019). This result suggests a phase change from water to vapor within the shallowest part of the hydrothermal system due to a pressure decrease after the phreatic eruption. An effect of compaction, which depends on the rheologies of subsurface rocks, can continue for a long time after a pressure drop. Todesco et al. (2014) described the process of compaction Δh with the following equation:

$$\Delta h = h_0 \frac{P_c A^{-1} t^b}{1 - \phi_0 + P_c A^{-1} t^b} \qquad (1)$$

where h_0 is the initial thickness of the compacting layer, ϕ_0 is the porosity, P_c is the pressure change, and t is the elapsed time in days. Additionally, A and b are empirically derived parameters that express the rheological properties of the compacting layer: A is a scalar associated with the magnitude of creep compaction, and b is related to the apparent viscosity of the system (Todesco et al., 2014). The initial thickness h_0 was set to 500 m, considering the structure beneath the bell-shaped conductor where the posteruptive deflation source is located (Seki et al., 2021; Figure 4), and the porosity ϕ_0 was set to 0.1 as a typical value used for simulations of hydrothermal systems (e.g., Tanaka et al., 2018). The other parameters were estimated by fitting, assuming that the LOS displacements were entirely in the vertical direction. The values of the parameters with error ranges in parentheses are P_c = 0.91 (0.70–1.11) MPa, A = 596,514 (483,720–777,888) MPa·day^b, and b = 0.64 (0.61–0.67), which are similar to the values estimated in Campi Flegrei (Todesco et al., 2014). The obtained curves (dashed lines in Figure 3) fit well with the pattern of subsidence after the 2015 phreatic eruption. Although the validity of these parameters remains to be verified, the results indicate that compaction due to a decrease in pore pressure is a plausible process to explain subsidence at the ground surface.

Another possible cause of deflation is a thermoelastic response with cooling (e.g., Furuya, 2005; Wang and Aoki, 2019). However, most examples of thermoelastic responses are related to the cooling of intruded magma bodies. Narita et al. (2019) demonstrated that the temperature change in the thermoelastic response expected from the posteruptive deflation after the 2014 phreatic eruption of Ontake volcano, Japan, was too large for the shallow part (500 m in depth) of the volcano. They concluded that the thermoelastic response is not a major factor contributing to deflation in Ontake volcano. The 2015 phreatic eruption of Hakone volcano was very small in scale, and significant temperature changes were unlikely to have happened in the coexisting vapor–liquid hydrothermal system, where the temperature change was buffered by the release of latent heat due to the condensation of water vapor (e.g., Ingebritsen et al., 2006). Therefore, the thermoelastic process is unlikely to be a major factor in the deflation of Hakone volcano.

The continuing deflation process means that the sealing ability has not been restored yet since the 2015 phreatic eruption of Hakone volcano. If compaction continues according to Equation (1), subsidence of approximately 5 mm/yr is predicted even 100 years after the eruption. However, if the sealing ability is restored as a result of mineral crystallization or other factors and the pressure starts to increase, this deflation will terminate shortly. Therefore, it is important to monitor the displacement at the ground surface to assess the pressure conditions of the hydrothermal system and the risk of future phreatic eruptions.

Acknowledgments, Samples, and Data

We would like to thank Dr. Teruyuki Kato of Taisho University for his helpful comments. We also thank Dr. John Stix and an anonymous reviewer for their constructive comments. This research was funded by JSPS KAKENHI grant numbers 19K04005 and 21H04602. ALOS-2/PALSAR-2 data were provided by JAXA. The processed data and geodetic modeling results are available on Zenodo (https://doi.org/10.5281/zenodo.5014834).

References

Berardino, P., Fornaro, G., Lanari, R., & Sansosti, E. (2002). A new algorithm for surface deformation monitoring based on small baseline differential SAR interferograms. *IEEE Transactions on Geoscience and Remote Sensing*, *40*(11), 2375–2383. https://doi.org/10.1109/TGRS.2002.803792

Costantini, M. (1998). A novel phase unwrapping method based on network programming. *IEEE Transactions on Geoscience and Remote Sensing*, *36*(3), 813–821. https://doi.org/10.1109/36.673674

Doke, R., Harada, M., Mannen, K., Itadera, K., & Takenaka, J. (2018). InSAR analysis for detecting the route of hydrothermal fluid to the surface during the 2015 phreatic eruption of Hakone Volcano, Japan. *Earth, Planets and Space*, *70*, 63. https://doi.org/10.1186/S40623-018-0834-4

Fujiwara, S., Nishimura, T., Murakami, M., Nakagawa, H., Tobita, M., & Rosen, P. A. (2000). 2.5-D surface deformation of M6.1 earthquake near Mt Iwate detected by SAR interferometry. *Geophysical Research Letters*, *27*(14), 2049-2052. https://doi.org/10.1029/1999GL011291

Fournier, R.O. (1999). Hydrothermal processes related to movement of fluid from plastic into brittle rock in the magmatic-epithermal environment. *Economic Geology*, *94*(8), 1193–1211. https://doi.org/10.2113/gsecongeo.94.8.1193

Furukawa, R., Ishizuka, Y., Yamasaki, S., Mannen, K., Nagai, M., Miwa, T., et al. (2015). Pyroclastic fall deposit of 2015 eruption from Hakone volcano, Japan. *Programme and Abstracts the Volcanological Society of Japan*, *2015*, P93. https://doi.org/10.18940/vsj.2015.0_191 (in Japanese)

Furuya, M. (2005). Quasi-static thermoelastic deformation in an elastic half-space: Theory and application to InSAR observations at Izu-Oshima volcano, Japan. *Geophysical Journal International*, *161*(1), 230–242. https://doi.org/10.1111/j.1365-246x.2005.02610.x

Geological Society of Japan (2007). *Geological leaflet 1 Hakone Volcano.* Tokyo: Geological Society of Japan. (in Japanese)

Goldstein, R.M., & Werner, C.L. (1998). Radar interferogram filtering for geophysical applications. *Geophysical Research Letters*, *25*(21), 4035–4038. https://doi.org/10.1029/1998gl900033

Hamling, I.J., Williams, C.A., & Hreinsdóttir, S. (2016). Depressurization of a hydrothermal system following the August and November 2012 Te Maari eruptions of Tongariro, New Zealand. *Geophysical Research Letters*, *43*(1), 168–175. https://doi.org/10.1002/2015gl067264

Harada, M., Doke, R., Mannen, K., Itadera, K., & Satomura, M. (2018). Temporal changes in inflation sources during the 2015 unrest and eruption of Hakone volcano, Japan. *Earth, Planets and Space*, *70*, 152. https://doi.org/10.1186/S40623-018-0923-4

Himematsu, Y., Ozawa, T., & Aoki, Y. (2020). Coeruptive and posteruptive crustal deformation associated with the 2018 Kusatsu-Shirane phreatic eruption based on PALSAR-2 time series analysis. *Earth, Planets and Space*, *72*, 116. https://doi.org/10.1186/s40623-020-01247-6

Honda, R., Yukutake, Y., Morita, Y., Sakai, S. I., Itadera, K., & Kokubo, K. (2018). Precursory tilt changes associated with a phreatic eruption of the Hakone volcano and the corresponding source model. *Earth, Planets and Space*, *70*, 117. https://doi.org/10.1186/s40623-018-0887-4

Ingebritsen, S.E., Sanford, W.E., & Neuzil, C.E. (2006). *Groundwater in geologic processes, 2nd edition*. Cambridge: Cambridge University Press.

Kobayashi, M. (2008). Eruption History of the Hakone Central Cone Volcanoes, and Geographical Development Closely Related to Eruptive Activity in the Hakone Caldera. *Research Report of the Kanagawa Prefectural Museum, Natural History*, *13*, 43–60. (in Japanese with English abstract)

Kobayashi, M., Mannen, K., Okuno, M., Nakamura, T., & Hakamata, K. (2006). The Owakidani tephra group: A newly discovered post-magmatic eruption product of Hakone Volcano, Japan. *Bulletin of the Volcanological Society of Japan*, *51*, 245–256. https://doi.org/10.18940/kazan.51.4_245 (in Japanese with English Abstract)

Kobayashi, T., Morishita, Y., & Munekane, H. (2018). First detection of precursory ground inflation of a small phreatic eruption by InSAR. *Earth and Planetary Science Letters*, *491*, 244–254. https://doi.org/10.1016/j.epsl.2018.03.041

Komori, S., Kagiyama, T., Utsugi, M., Inoue, H., & Azuhata, I. (2013). Two-dimensional resistivity structure of Unzen Volcano revealed by AMT and MT surveys. *Earth, Planets and Space*, *65*(7), 759–766. https://doi.org/10.5047/eps.2012.10.005

Lévy, L., Gibert, B., Sigmundsson, F., Flóvenz, Ó., Hersir, G., Briole, P., & Pezard, P. (2018). The role of smectites in the electrical conductivity of active hydrothermal systems: Electrical properties of core samples from Krafla volcano, Iceland. *Geophysical Journal International*, *215*(3), 1558–1582. https://doi.org/10.1093/gji/ggy342

Mannen, K., Abe, Y., Daita, Y., Doke, R., Harada, M., Kikugawa, G., et al. (2021). Volcanic unrest at Hakone volcano after the 2015 phreatic eruption: Reactivation of a ruptured hydrothermal system? *Earth, Planets and Space*, *73*, 80. https://doi.org/10.1186/s40623-021-01387-3

Mannen, K., Tanada, T., Jomori, A., Akatsuka, T., Kikugawa, G., Fukazawa, Y., et al. (2019). Source constraints for the 2015 phreatic eruption of Hakone volcano, Japan, based on geological analysis and resistivity structure. *Earth, Planets and Space*, *71*, 135. https://doi.org/10.1186/s40623-019-1116-5

Mannen, K., Yukutake, Y., Kikugawa, G., Harada, M., Itadera, K., & Takenaka, J. (2018). Chronology of the 2015 eruption of Hakone volcano, Japan: Geological background, mechanism of volcanic unrest and disaster mitigation measures during the crisis. *Earth, Planets and Space*, *70*, 68. https://doi.org/10.1186/s40623-018-0844-2

Mogi, K. (1958). Relations between the eruptions of various volcanoes and the deformations of the ground surfaces around them. *Bulletin of the Earthquake Research Institute*, *36*, 99–134.

Narita, S., & Murakami, M. (2018). Shallow hydrothermal reservoir inferred from post-eruptive deflation at Ontake Volcano as revealed by PALSAR-2 InSAR. *Earth, Planets and Space*, *70*, 191. https://doi.org/10.1186/s40623-018-0966-6

Narita, S., Murakami, M., & Tanaka, R. (2019). Quantitative relationship between plume emission and multiple deflations after the 2014 phreatic eruption at Ontake volcano, Japan. *Earth, Planets and Space*, *70*, 145. https://doi.org/10.1186/s40623-019-1124-5

Nurhasan, Ogawa, Y., Ujihara, N., Tank, S.B., Honkura, Y., Onizawa, S.Y., et al. (2006). Two electrical conductors beneath Kusatsu–Shirane volcano, Japan, imaged by audiomagnetotellurics, and their implications for the hydrothermal system. *Earth, Planets and Space*, *58*(8), 1053–1059. https://doi.org/10.1186/bf03352610

Okada, Y. (1985). Surface deformation due to shear and tensile faults in a half-space. *Bulletin of the Seismological Society of America*, *75*(4), 1135–1154. https://doi.org/10.1785/BSSA0750041135

Pavlis, N.K., Holmes, S.A., Kenyon, S.C., & Factor, J.K. (2012). The development and evaluation of the Earth Gravitational Model 2008 (EGM2008). *Journal of Geophysical Research: Solid Earth*, *117*(B4). https://doi.org/10.1029/2011JB008916

Pellerin, L., Johnston, J.M., & Hohmann, G.W. (1996). A numerical evaluation of electromagnetic methods in geothermal exploration. *Geophysics*, *61*(1), 121–130. https://doi.org/10.1190/1.1443931

Rosenqvist, A., Shimada, M., Suzuki, S., Ohgushi, F., Tadono, T., Watanabe, M., et al. (2014). Operational performance of the ALOS global systematic acquisition strategy and observation plans for ALOS-2 PALSAR-2. *Remote Sensing of Environment*, *155*, 3–12. https://doi.org/10.1016/j.rse.2014.04.011

Seki, K., Kanda, W., Mannen, K., Takakura, S., Koyama, T., Noguchi, R., et al. (2021). Imaging the Source Region of the 2015 Phreatic Eruption at Owakudani, Hakone Volcano, Japan, Using High-Density Audio-Frequency Magnetotellurics. *Geophysical Research Letters*, *48*(1). https://doi.org/10.1029/2020gl091568

Stix, J., & De Moor, J.M. (2018). Understanding and forecasting phreatic eruptions driven by magmatic degassing. *Earth, Planets and Space*, *70,* 83. https://doi.org/10.1186/s40623-018-0855-z

Tanaka, R., Hashimoto, T., Matsushima, N., & Ishido, T. (2018). Contention between supply of hydrothermal fluid and conduit obstruction: inferences from numerical simulations. *Earth, Planets and Space*, *70*, 72. https://doi.org/10.1186/s40623-018-0840-6

Todesco, M., Costa, A., Comastri, A., Colleoni, F., Spada, G., & Quareni, F. (2014). Vertical ground displacement at Campi Flegrei (Italy) in the fifth century: Rapid subsidence driven by pore pressure drop. *Geophysical Research Letters, 41*(5), 1471–1478. https://doi.org/10.1002/2013gl059083

Tsuchiya, M., Mannen, K., Kobayashi, M., & Fukuoka, T. (2017). Two Types of Glass Shards within the Owakidani Tephra Group Deposit, Hakone Volcano: Constraints on Their Sources and Ages. *Bulletin of the Volcanological Society of Japan*, *62*(1), 23–30. https://doi.org/10.18940/kazan.62.1_23 (in Japanese with English Abstract)

Usui, Y., Ogawa, Y., Aizawa, K., Kanda, W., Hashimoto, T., Koyama, T., et al. (2017). Three-dimensional resistivity structure of Asama Volcano revealed by data-space magnetotelluric inversion using unstructured tetrahedral elements. *Geophysical Journal International*, *208*(3), 1359–1372. https://doi.org/10.1093/gji/ggw459

Wang, X., & Aoki, Y. (2019). Posteruptive Thermoelastic Deflation of Intruded Magma in Usu Volcano, Japan, 1992–2017. *Journal of Geophysical Research: Solid Earth*, *124*(1), 335–357. https://doi.org/10.1029/2018jb016729

Wang, X., Aoki, Y., & Chen, J. (2019). Surface deformation of Asama volcano, Japan, detected by time series InSAR combining persistent and distributed scatterers, 2014–2018. *Earth, Planets and Space*, *70*, 121. https://doi.org/10.1186/s40623-019-1104-9

Yoshimura, R., Ogawa, Y., Yukutake, Y., Kanda, W., Komori, S., Hase, H., et al. (2018). Resistivity characterisation of Hakone volcano, Central Japan, by three-dimensional magnetotelluric inversion. *Earth, Planets and Space*, *70*, 66. https://doi.org/10.1186/s40623-018-0848-y

Yukutake, Y., Abe, Y., & Doke, R. (2019). Deep Low-Frequency Earthquakes Beneath the Hakone Volcano, Central Japan, and their Relation to Volcanic Activity. *Geophysical Research Letters*, *46*(20), 11035–11043. https://doi.org/10.1029/2019gl084357

Yukutake, Y., Honda, R., Harada, M., Doke, R., Saito, T., Ueno, T., et al. (2017). Analyzing the continuous volcanic tremors detected during the 2015 phreatic eruption of the Hakone volcano. *Earth, Planets and Space*, *69*, 164. https://doi.org/10.1186/S40623-017-0751-Y

References From the Supporting Information

Jonsson, S. (2002). Fault Slip Distribution of the 1999 Mw 7.1 Hector Mine, California, Earthquake, Estimated from Satellite Radar and GPS Measurements. *Bulletin of the Seismological Society of America*, *92*(4), 1377–1389. https://doi.org/10.1785/0120000922

Marquardt, D.W. (1963). An Algorithm for Least-Squares Estimation of Nonlinear Parameters. *Journal of the Society for Industrial and Applied Mathematics*, *11*(2), 431–441. https://doi.org/10.1137/0111030

Mogi, K. (1958). Relations between the eruptions of various volcanoes and the deformations of the ground surfaces around them. *Bulletin of the Earthquake Research Institute*, *36*, 99–134. https://doi.org/10.1785/BSSA0750041135

Okada, Y. (1985). Surface deformation due to shear and tensile faults in a half-space. *Bulletin of the Seismological Society of America*, *75*(4), 1135–1154.

Welstead, S. (1999). *Fractal and Wavelet Image Compression Techniques (Vol. TT40)*. Bellingham, Washington: SPIE Optical Engineering Press.

Figure 1. Index map of Hakone volcano. The base map is a false-color image captured by ALOS/AVNIR-2 on 10 November 2006, and the red tones indicate vegetated areas. The areas enclosed by the rectangles indicate the analysis areas in this study.

Figure 2. Distribution of LOS velocities estimated from SBAS-InSAR time series analysis of ALOS-2/PALSAR-2 data; (**a**) path 126, (**b**) path 18, and (**c**) quasi-eastward and (**d**) quasi-upward components. The contour lines represent intervals of 100 m in height. The red circles represent locations mentioned in the text and Figure 3. The yellow circles (E) show the location of the 2015 eruption center. The red dashed line shows the area surrounded by the bell-shaped conductor at the height of 0 m (Yoshimura et al., 2018).

Figure 3. Time variation of the displacements at locations A–C in Figure 2 for (**a**) path 126 and (**b**) path 18. Locations A and B were selected on the caldera floor and the central cones of Hakone volcano, respectively. Location C is the site that shows the maximum velocity away from the satellite along the LOS in path 18. Positive and negative values indicate displacements toward and away from the satellite, respectively. Dashed lines are the lines of best fit assuming that compaction due to the pore pressure decreases (see text).

Figure 4. Schematic illustration of the shallow hydrothermal system beneath the central cones of Hakone volcano. The subsurface model is based on the conductivity structure and interpretation shown in Figure 4 of Seki et al. (2021), previous deformation sources proposed by Doke et al. (2018), and the results of the present study. During the 2015 phreatic eruption, the sealing layer was ruptured, and pressurized hydrothermal fluids migrated toward the shallower edifice. Posteruptive deflation might be caused by a pore pressure decrease in the hydrothermal reservoir due to fluid migration.

Table 1. Estimated Model Parameters.

Figure 1.

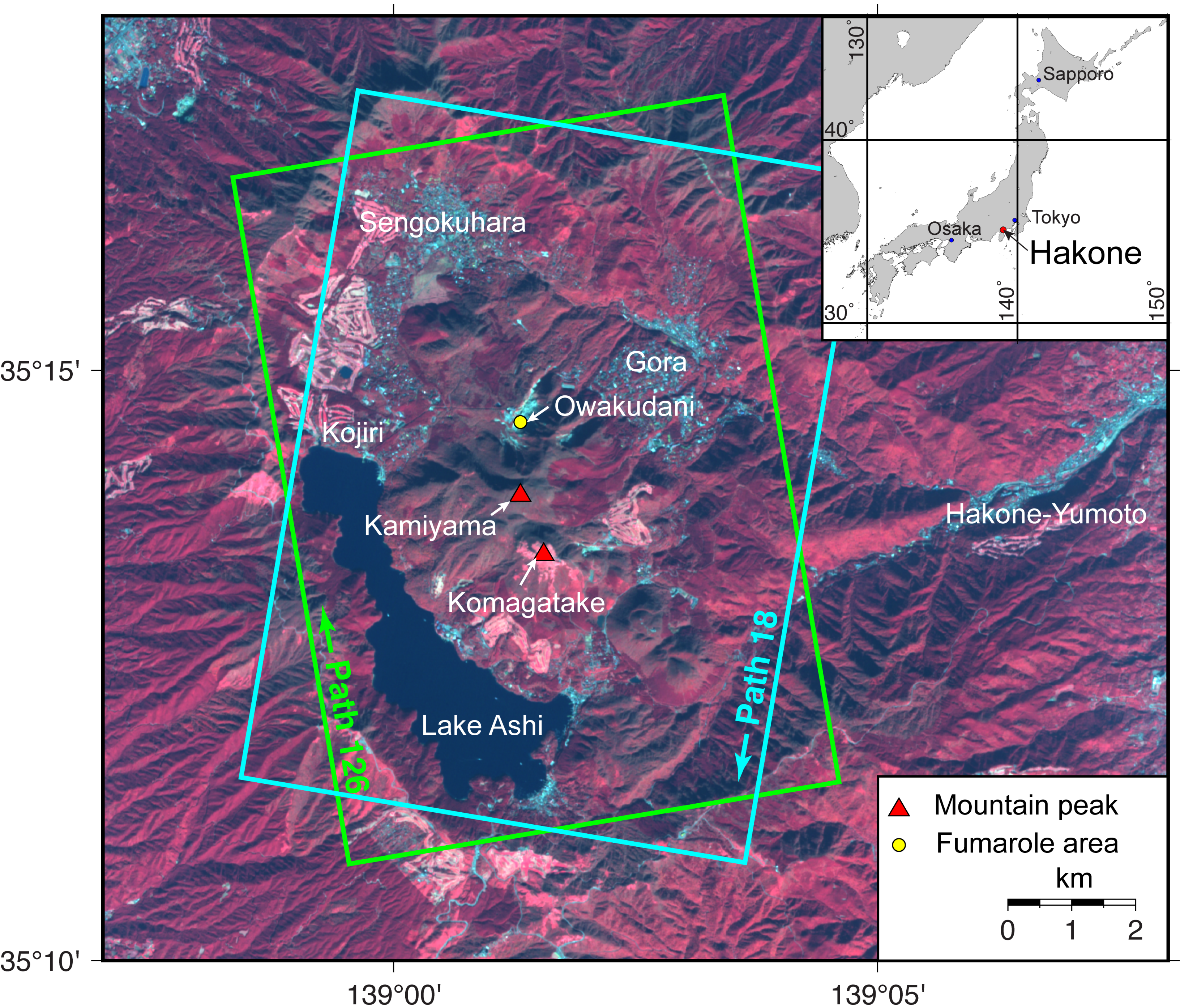

Sengokuhara
Gora
Owakudani
Kojiri
Kamiyama
Komagatake
Hakone-Yumoto
Lake Ashi
Path 126
Path 18
Sapporo
Tokyo
Osaka
Hakone
130°
140°
150°
40°
30°
Mountain peak
Fumarole area
km
0
1
2
35°15'
35°10'
139°00'
139°05'

Figure 2.

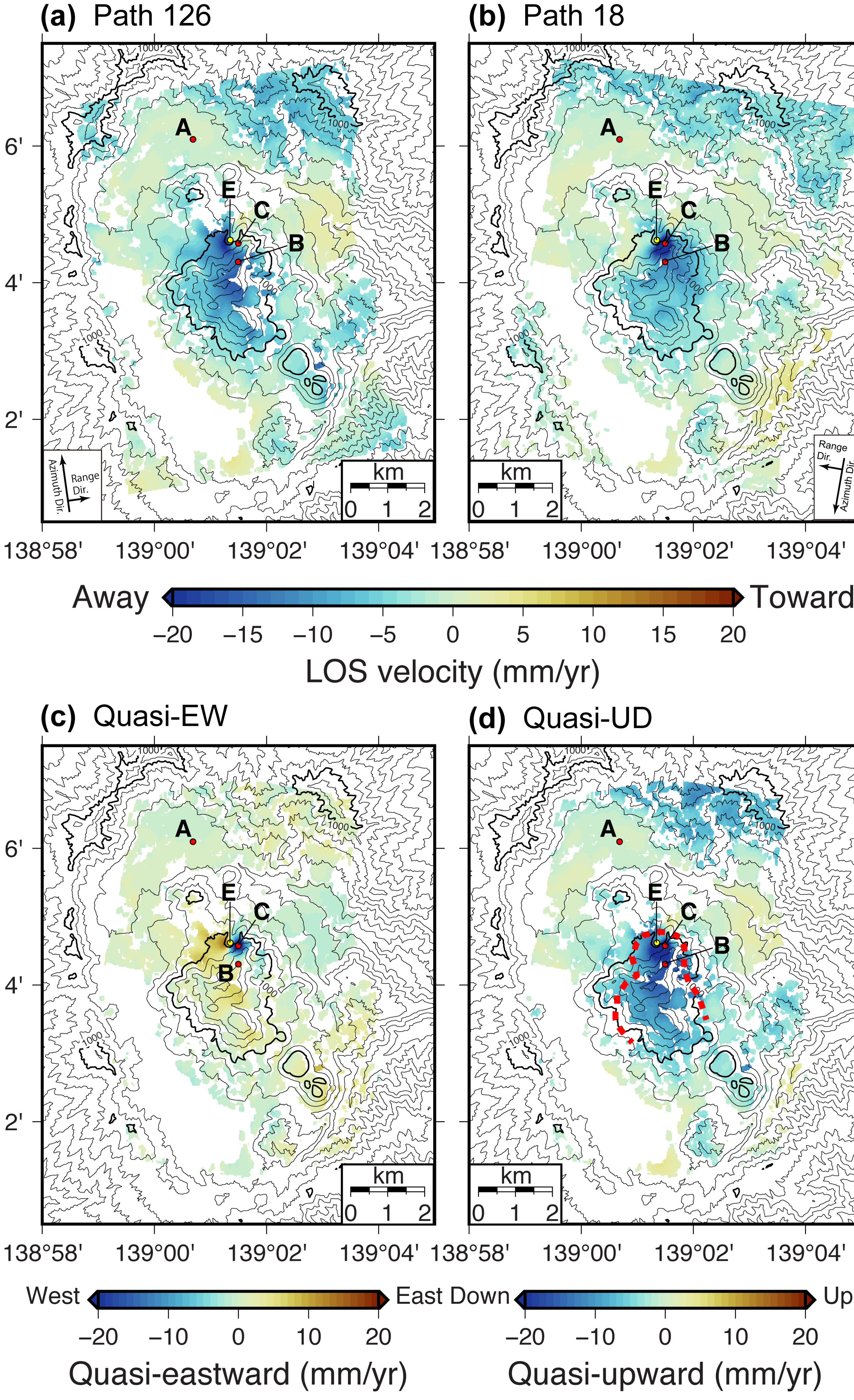

(a) Path 126
(b) Path 18
(c) Quasi-EW
(d) Quasi-UD
A
B
C
E
1000
35°16'
35°14'
35°12'
138°58'
139°00'
139°02'
139°04'
km
0 1 2
Azimuth Dir.
Range Dir.
Away
Toward
−20 −15 −10 −5 0 5 10 15 20
LOS velocity (mm/yr)
West
East
Down
Up
−20 −10 0 10 20
Quasi-eastward (mm/yr)
Quasi-upward (mm/yr)

Figure 3.

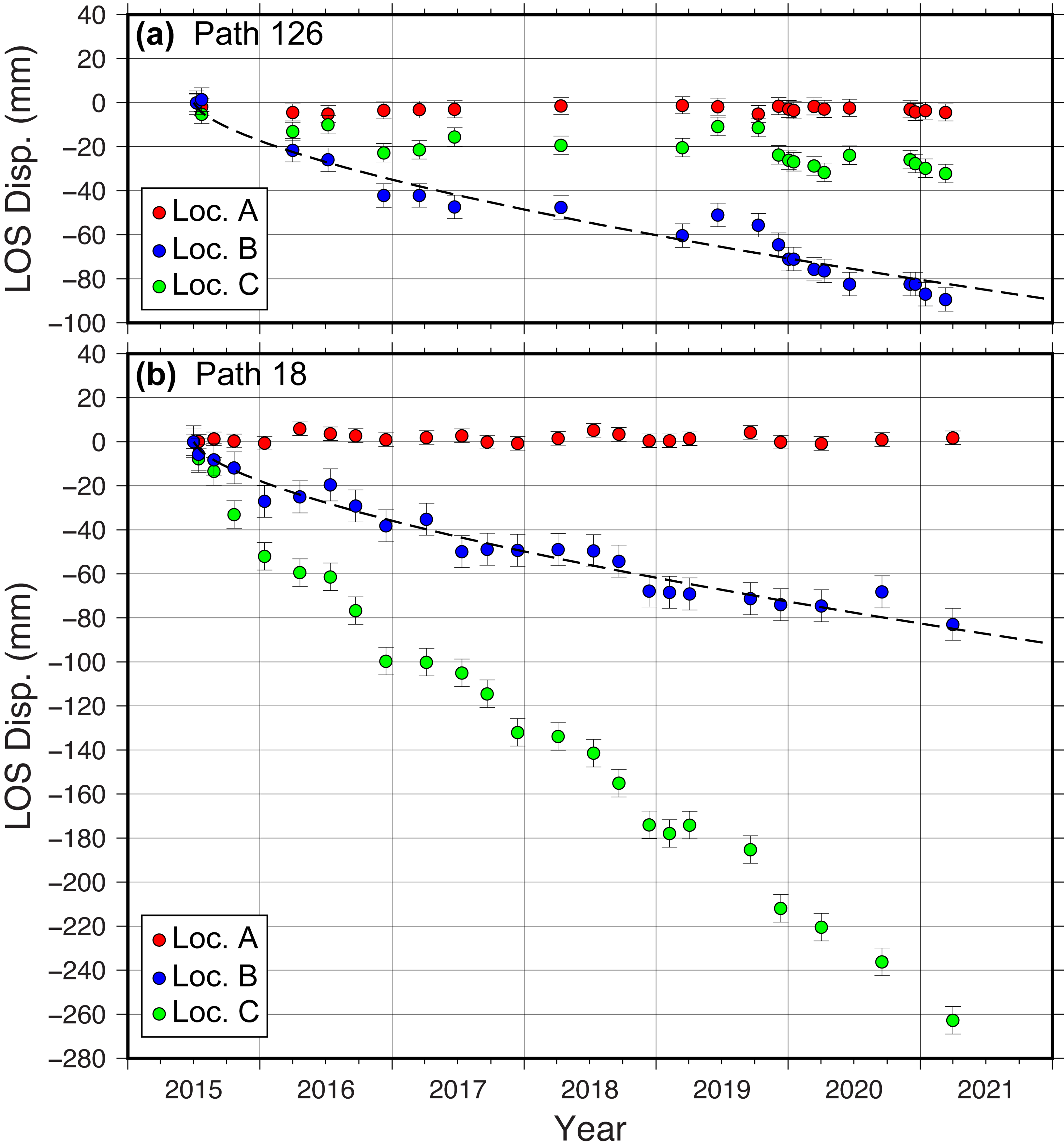

(a) Path 126
Loc. A
Loc. B
Loc. C
LOS Disp. (mm)
40
20
0
−20
−40
−60
−80
−100
(b) Path 18
Loc. A
Loc. B
Loc. C
LOS Disp. (mm)
40
20
0
−20
−40
−60
−80
−100
−120
−140
−160
−180
−200
−220
−240
−260
−280
2015
2016
2017
2018
2019
2020
2021
Year

Figure 4.

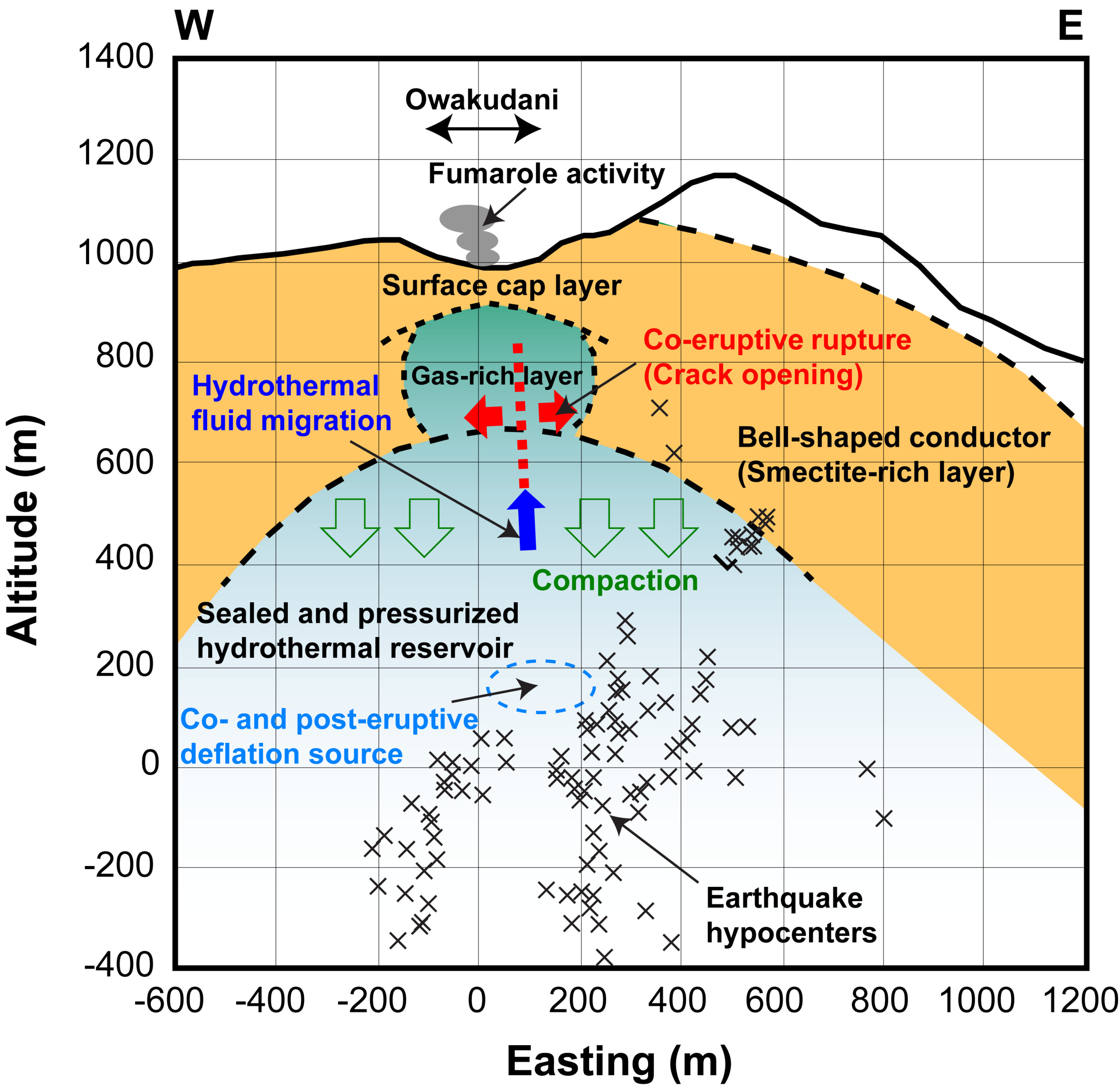
W
E
Owakudani
Fumarole activity
Surface cap layer
Gas-rich layer
Co-eruptive rupture
(Crack opening)
Hydrothermal
fluid migration
Bell-shaped conductor
(Smectite-rich layer)
Compaction
Sealed and pressurized
hydrothermal reservoir
Co- and post-eruptive
deflation source
Earthquake
hypocenters
Altitude (m)
Easting (m)
1400
1200
1000
800
600
400
200
0
-200
-400
-600
-400
-200
0
200
400
600
800
1000
1200

Table 1. *Estimated Model Parameters.*

	Model A [Point source deflation]	Model B [Sill deflation]
Longitude (°) [a]	139.0242 (0.0007)	139.0289 (0.0005) [b]
Latitude (°) [a]	35.2372 (0.0006)	35.2250 (0.0006) [b]
Altitude (m) [c]	211.0 (64.7)	95.0 (42.9)
Volume change rate (m^3/yr)	-5.96×10^4 (2.76×10^4)	-6.54×10^4 (5.78×10^3) [d]
Length (m)	–	2392.2 (94.0)
Width (m)	–	246.2 (15.4)
Strike (°)	–	339.1 (1.2)
Opening rate (m/yr)	–	−0.111 (0.005)
RMS Path 126 (mm/yr)	2.525	2.305
RMS Path 18 (mm/yr)	2.358	2.255
RMS Total (mm/yr)	2.444	2.280
AIC	3662	3574

Note: Standard errors are given in parentheses.

[a] The longitude and latitude are given in WGS-84 coordinates.

[b] The coordinates for Model B indicate the southernmost point of the sill model.

[c] The altitude is the height above sea level, corrected from the originally estimated ellipsoidal height.

[d] The volume change rate for Model B was calculated from the length, width, and opening of the sill model.

AGU PUBLICATIONS

Geophysical Research Letters

Supporting Information for

Observing posteruptive deflation of hydrothermal system using InSAR time series analysis: An application of ALOS-2/PALSAR-2 data on the 2015 phreatic eruption of Hakone volcano, Japan

by R. Doke[1], K. Mannen[1], and K. Itadera[1]

[1] Hot Springs Research Institute of Kanagawa Prefecture, 586 Iriuda, Odawara, Kanagawa 250-0031, Japan.

Contents of this file

Text S1
Figures S1 to S5
Table S1

Introduction

Test S1 describes the methods and results of model inversion. Figure S1 shows the temporal and spatial baselines for the SBAS-InSAR time series analysis of ALOS-2/PALSAR-2 data. Figures S2 and S3 show the results of the model inversion. Figures S4 and S5 show the standard deviations of and tradeoffs among the model parameters for the point source and sill deflation models, respectively. Table S1 gives the ALOS-2/PALSAR-2 data used in this study.

Text S1. Model Inversion

Model inversion was performed to explain the surface velocity distributions obtained from the SBAS-InSAR time series analysis. Before the modeling, the surface velocity maps (Figure 2) were subsampled using the quadtree-partitioning algorithm (Jonsson, 2002; Welstead, 1999) to reduce the influence of noise. In the algorithm, a scene is divided into four quadrants, and the root mean square (RMS) of the surface velocity for each quadrant was calculated. If the RMS of the quadrant exceeds a given threshold, the quadrant is divided into four new quadrants, and the RMS of each is calculated and again compared with the threshold. The subdividing process was continued until the RMS of the surface velocity dropped below the threshold or a given maximum number of subdivision steps was reached. In this study, the RMS threshold was set to 1 mm/yr, and the maximum number of steps was set to 6. Because the size of the smallest quadrant (a mesh of approximately 300 m in the E–W direction) is comparable to or slightly larger than the observed significant local displacements, such as the landslide in Owakudani, such observations can be expected to produce no significant effect on this model evaluation, which focuses on large-scale displacements. The subsampled datasets consist of 346 and 339 points for paths 126 and 18, respectively (Figures S2(a), (b) and S3 (a), (b)).

Here, we employed two deflation source models: a point pressure source model (Mogi, 1958) and a rectangular sill model (tensile fault model by Okada, 1985) in a semi-infinite elastic crust. To consider the effect of topography, the elevations of observed points in datasets were compensated. The optimal parameters of the models were estimated using a modeling tool in ENVI SARscape, which employs the nonlinear inversion algorithm based on the Levenberg–Marquardt least-squares approach (Marquardt, 1963). The offsets of the datasets were also estimated assuming a linear ramp, along with the parameters of the model. After the best-fit parameters were obtained, the standard deviations of each parameter were determined from the results of another 250 iterations. The standard errors were calculated as the standard deviations divided by the square root of the number of iterations. Additionally, the tradeoff relationships among the parameters were visualized based on the iteration results (Figures S4 and S5).

Figures S2 and S3 show the surface velocities simulated by the optimal point source and sill deflation models, respectively. The optimal parameters estimated from the model inversion are given in Table 1 with their standard errors.

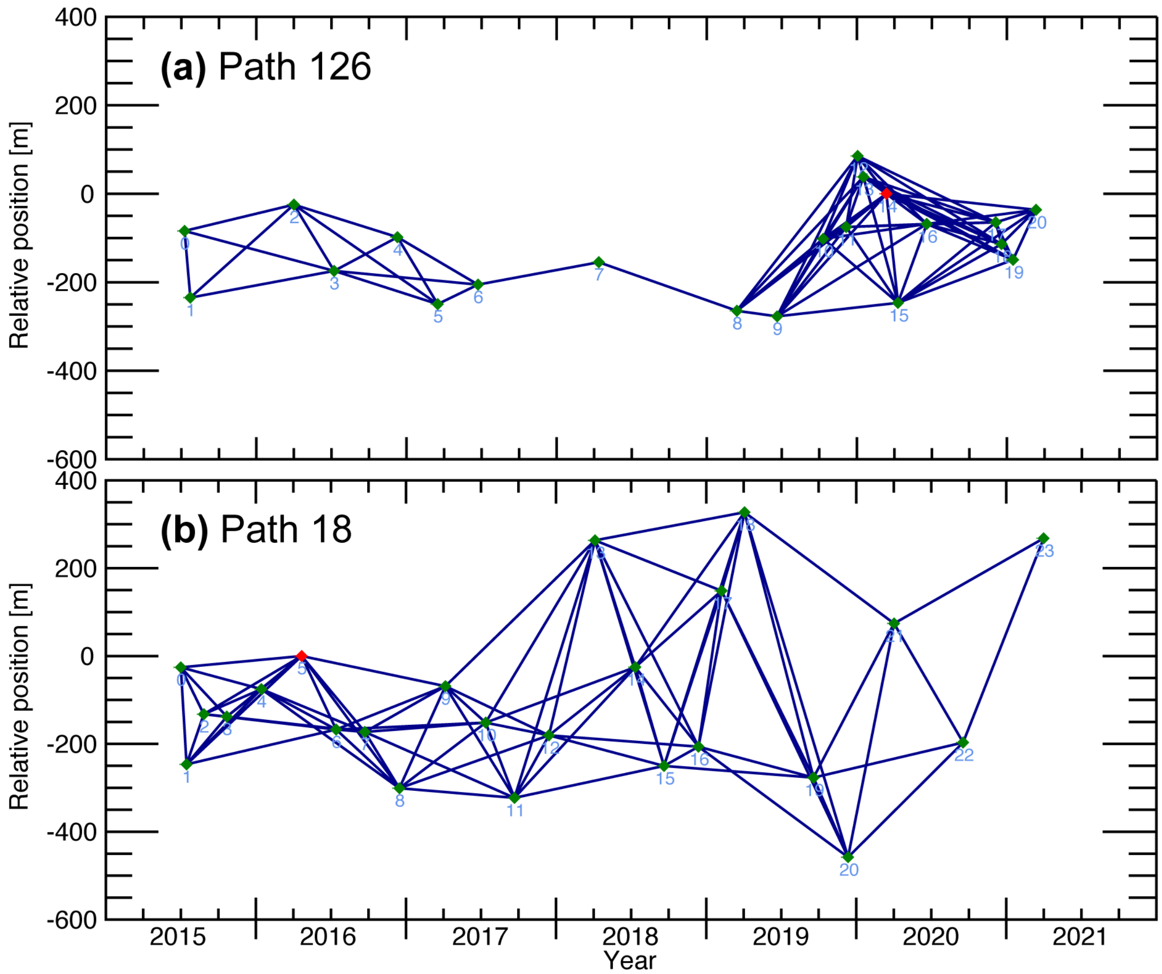

Figure S1. Temporal and spatial baselines for the SBAS-InSAR time series analysis of ALOS-2/PALSAR-2 data from (a) path 126 and (b) path 18. Red points show the super primary scenes used for the analysis, which the software selected as the scenes with the highest number of connections to other scenes.

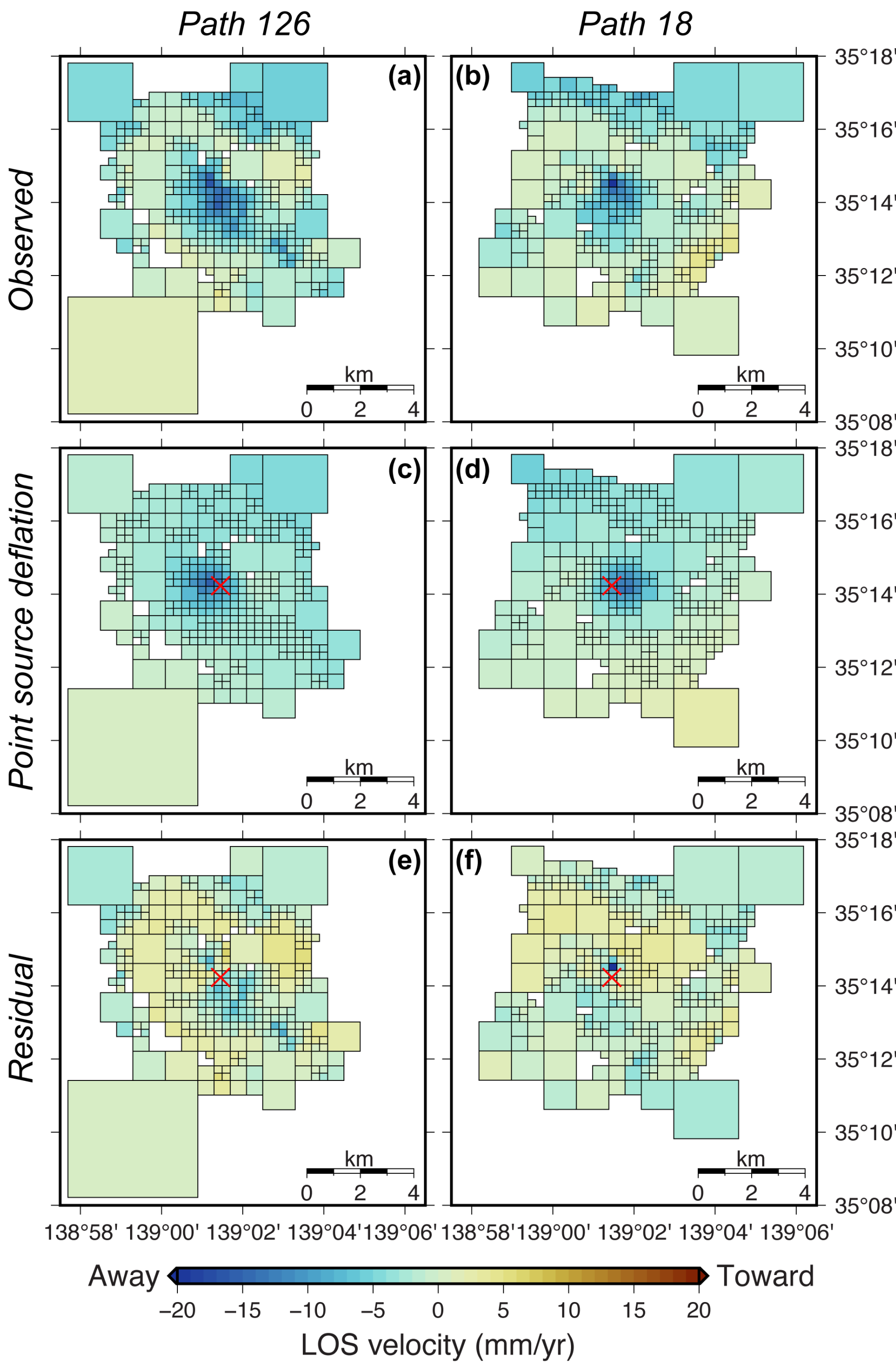

Figure S2. Results of inversion by the point source deflation model. Subsampled velocity datasets prepared by quadtree-partitioning for (a) path 126 and (b) path 18. Simulated velocities for (c) path 126 and (d) path 18, and residuals for (e) path 126 and (f) path 18. The red crosses indicate the locations of the estimated point source. The parameters and standard errors of the models are listed in Table 1.

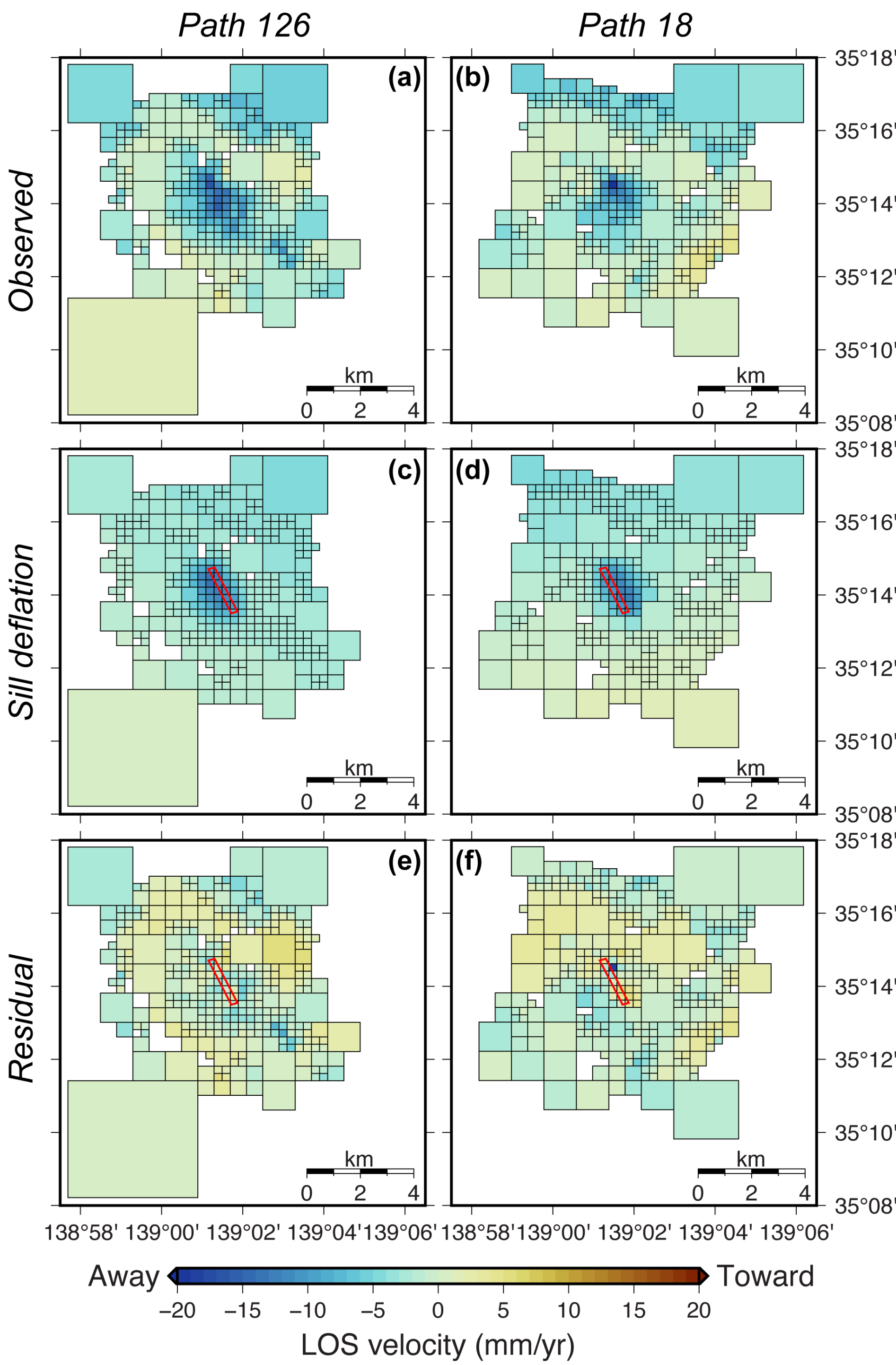

Figure S3. Results of inversion by the sill deflation model. Subsampled velocity datasets prepared by quadtree-partitioning for (a) path 126 and (b) path 18. Simulated velocities for (c) path 126 and (d) path 18, and residuals for (e) path 126 and (f) path 18. The red rectangles indicate the locations of the estimated sill model. The parameters and standard errors of the models are listed in Table 1.

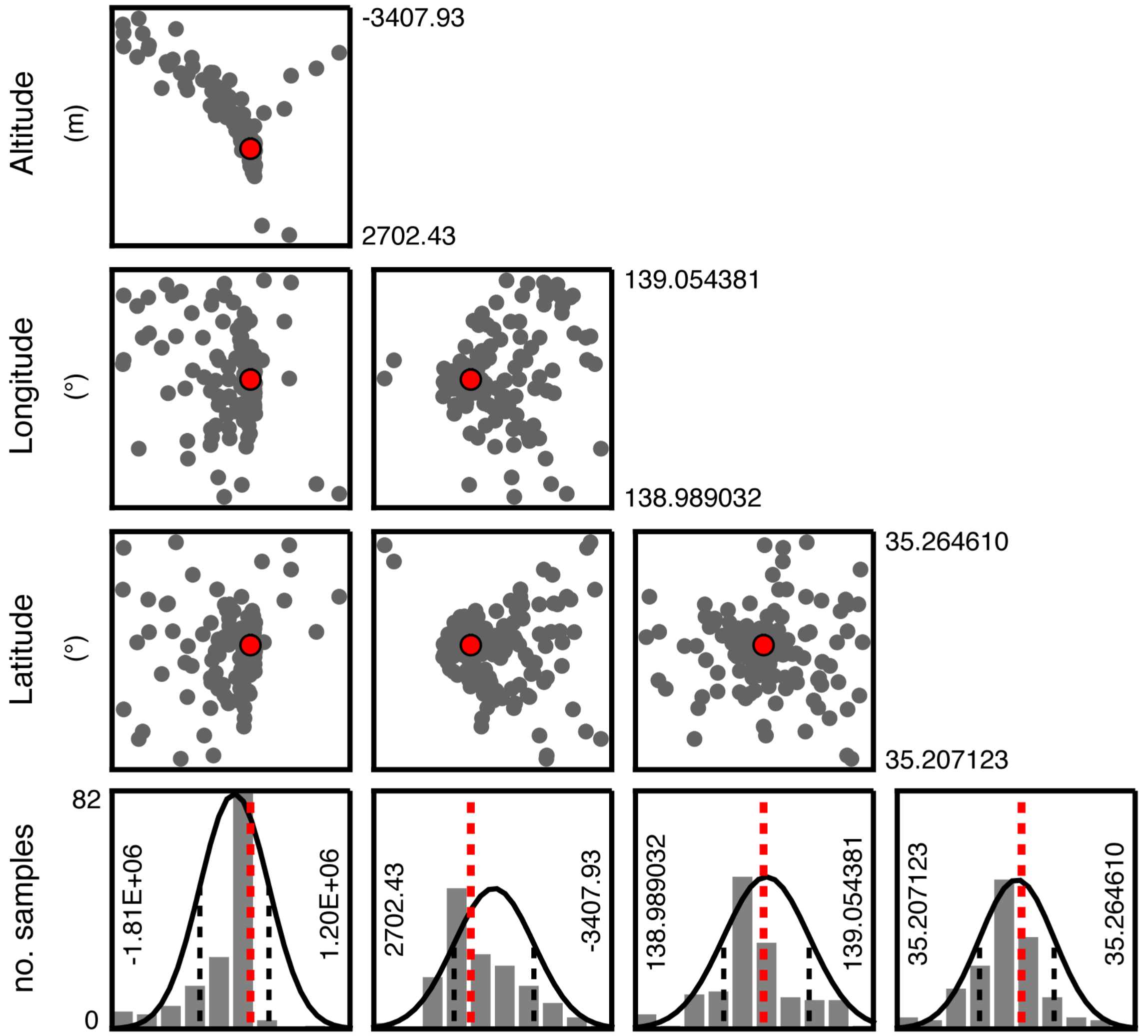

	Volume change rate (m^3/yr)	Altitude (m)	Longitude (°)	Latitude (°)
Best-fit	-5.96×10^4	210.97	139.024217	35.237176
Mean	-2.62×10^5	-383.48	139.025004	35.236028
St. dev.	4.36×10^5	1023.62	0.011741	0.009010

Figure S4. Standard deviation (histograms) and tradeoffs (scatter plots) between the model parameters for the point source deflation model. Red points and red dashed lines show the optimal parameters for the model.

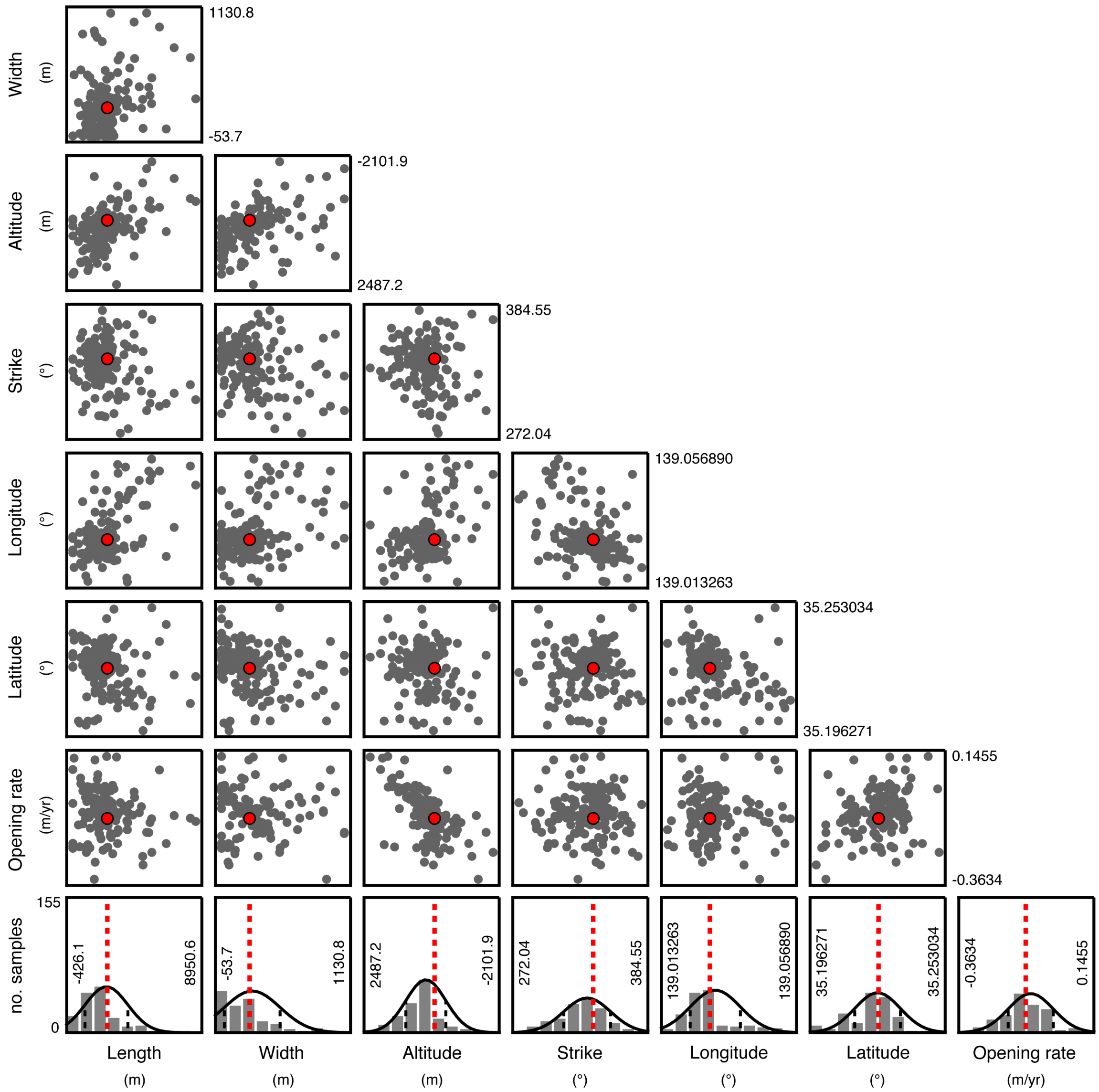

	Length (m)	Width (m)	Altitude (m)	Strike (°)	Longitude (°)	Latitude (°)	Opening rate (m/yr)
Best-fit	2392.2	246.2	95.0	339.07	139.028902	35.225021	-0.1112
Mean	2331.3	269.4	388.8	334.00	139.030657	35.224627	-0.0923
St. dev.	1486.8	244.2	678.1	19.49	0.008112	0.009587	0.0849

Figure S5. Standard deviation (histograms) and tradeoffs (scatter plots) between the model parameters for the sill deflation model. Red points and red dashed lines show the optimal parameters for the model.

Path 126 (Ascending, right-looking)		Path 18 (Descending, right-looking)	
Observation Date	Position [m] [a]	Observation Date	Position [m] [a]
10 July 2015	−84.0080	2 July 2015	−25.8004
24 July 2015	−234.737	16 July 2015	−246.664
1 April 2016	−24.5921	27 August 2015	−132.418
8 July 2016	−174.293	22 October 2015	−137.915
9 December 2016	−98.1012	14 January 2016	−75.3610
17 March 2017	−249.382	21 April 2016 [b]	0
23 June 2017	−205.337	14 July 2016	−167.343
13 April 2018	−154.725	22 September 2016	−172.853
15 March 2019	−264.493	15 December 2016	−300.976
21 June 2019	−277.087	6 April 2017	−68.6881
11 October 2019	−101.863	13 July 2017	−151.660
6 December 2019	−75.1073	21 September 2017	−322.930
3 January 2020	85.4325	14 December 2017	−180.590
17 January 2020	38.2575	5 April 2018	263.321
13 March 2020 [b]	0	12 July 2018	−25.3933
10 April 2020	−246.522	20 September 2018	−250.212
19 June 2020	−68.3064	13 December 2018	−206.409
4 December 2020	−64.6116	7 February 2019	148.452
18 December 2020	−113.811	4 April 2019	327.216
15 January 2021	−149.254	19 September 2019	−276.874
12 March 2021	−36.3006	12 December 2019	−458.007
		2 April 2020	74.0828
		17 September 2020	−196.891
		1 April 2021	268.010

[a] Positions are perpendicular baseline lengths between the scene and the super primary scene.

[b] The scenes used as the super primary scenes, which the software selected as the scenes with the highest number of connections to other scenes.

Table S1. ALOS-2/PALSAR-2 data used in this study.